View metadata, citation and similar papers at core.ac.uk
brought to you by CORE
provided by Apollo

Folding a Ridge-Spring

K A Seffen

Advanced Structures Group, Department of Engineering, University of Cambridge, CB2 1PZ

kas14@cam.ac.uk

Highlights:

- A folded ridge-spring has different physical dependencies than a tape-spring.
- Simple energy models consider cylindrical bending with boundary layer edge effects.
- Predictions of folded radius and bending moment compare well to finite elements.
- A folded ridge-spring can be designed more effectively than a tape-spring.

Abstract

A ridge-spring is a thin-walled bent strip with flat side panels. It may be folded elastically along its length, to create a localised hinge region of mostly uniform cylindrical curvature and bending moment, which do not vary with the fold angle of hinge. A simple analysis shows a common grouping in closed-form expressions; $\alpha^{4/3} \cdot (b/t)^{1/3}$, where α is the pitch angle of the ridge line, b is the strip width and t its thickness. More accurate calculations of the hinge curvature and moment confirm the robustness of simpler expressions, which are compared to data obtained from finite element simulations. It is shown that, for many initial geometries, theoretical predictions of curvature and moment are typically within 10% of the computational results—which project the same dimensional performance. We also compare a ridge-spring to a more familiar tape-spring of equal cross-sectional proportions. For moderate pitch angles and relatively small thicknesses, it is shown that a ridge-spring has a higher folded hinge curvature and bending moment, comparatively, which may prove attractive for certain applications.

Keywords: buckling, elastic material, structures, finite elements, energy methods

Major nomenclature

α: pitch angle

θ: hinge fold angle

κ^*: hinge curvature ($= 1/r^*$)

$\bar{\kappa}^*$: dimensionless hinge curvature ($= b/r^*$)

μ: cylinder bending term ($= (r \cdot t)^{1/2}/[3(1-\nu^2)]^{1/4}$)

ν: Poisson's ratio

ξ: cylinder bending term ($= b/2\mu$)

ϕ: dimensionless edge rotation ($= \mu\psi$)

$\chi_{x,y}$: changes of curvature

ψ: edge rotation

A: constant equal to $[3(1-\nu^2)]^{1/4}$

b: arc-width of ridge-spring

D: flexural rigidity ($= Dt^3/12(1-\nu^2)$)

E: Young's modulus

$M_{x,y}$: bending moments

$M_{0,1,2}$: edge bending moments

M^*: hinge bending moment

$\bar{M}^*$: dimensionless hinge moment ($= M/D\alpha$)

m: dimensionless edge moment ($= \mu M/2D$)

r: general hinge radius

r^*: folded hinge radius

R: tape-spring transverse radius

t: through-thickness

U_{T}: tape-spring strain energy

U_{R}: ridge-spring strain energy

U_{M}: ridge-spring modified strain energy

U_{E}: ridge-spring exact strain energy

x: transverse coordinate

y: longitudinal coordinate

1 Introduction

Figure 1(a) shows a variety of straight, thin-walled strips, of lengths at least five times their width. They are made from metal or paper card, and their cross-sections have one of three types of symmetrical profile.

The familiar carpenter's tape, or "tape-spring", has a uniform transverse curvature. The paper strips are made by folding originally flat strips along a middle line, to form a sharp ridge line of a particular pitch angle, connected to inclined side panels. The copper-beryllium (CuBe) strip—complete with end blocks—has a more rounded ridge separating its side panels, after age-hardening a flat strip in a mould of the same profile.

When the metal strips are bent along their lengths, they buckle into localised, folded regions—*hinges*—of approximately the same extent, see Fig. 1(b): the strips are held in place by equal and opposite collinear forces applied (out of view) to the straight ends.

The paper ridges in Fig. 1(c) fold similarly but their hinges have different sizes. In all cases, the central dorsal line along the strip is in tension; if bending proceeds in the opposite sense, each ridged strip collapses into a sharp, often damaged vertex—not of interest here; see [1] for more details. A tape-spring, however, folds the same, whatever the bending direction.

A finite element analysis of folding is carried out in Fig. 2 for a tape-spring and a concentrated ridge of the same arc-width and "angularity" as indicated, inset; they both have the same length and wall thickness. Equal and opposite end-wise couples, M, are applied to the ends of each strip, to cause pure bending.

The early deformation is discussed in Section 2 but notice how M remains constant once each hinge has formed, and does not depend on the angle of inclination, θ, between the strip ends. Both hinges are clearly cylindrical in side-view; their curvatures do not change with θ—only the arc-length they envelope; and outside the hinge, the strips are practically straight.

Such uniform response is well known for a carpenter's tape; and bespoke tape-springs have been used for designing elastically-driven deployable structures [2].

Furthermore, the curvature of a tape-spring hinge is (approximately) the same as its natural cross-section, when bent in either direction. A first calculation of this remarkable property was performed by Rimrott [3], who assumed a *developable* hinge shape of uniform changes in curvature, within a simple energetic framework.

The origin of the uniformity of hinge properties is less obvious. The author suggested the hinge to be a type of *propagating instability* [4] in which only the arc-length of hinge along the strip changes *i.e.* propagates, as θ is changed.

The application of the *Maxwell Construction* [5] provides further validation, and enables the calculation of the fixed propagating load *i.e.* end-wise (thus hinge) moment and fixed deformation *i.e.* constant hinge curvature, from the general bending response under uniform moments—the complete equilibrium load path.

This proposition was tested for ridged specimens in [6, 7]. Their cross-sections assumed an ever-decreasing

width of ridge, from full (tape-spring) to nearly singular width, but not quite "reaching" the geometry in Fig. 2.

Propagation in the sense of Maxwell's Construction was formally validated within a numerical scheme because of the lengthy closed-form expressions for the general bending response [6, 7]: and the systematic variation of hinge properties from concentrating the original transverse curvature was found to correlate well with experimental- and computational results.

Inspired by Rimrott's approach, they also determined closed-form expressions for the uniform hinge properties in [6, 7], assuming, as Rimrott did for tape-springs, a developable deformation: their compactness stems from the constancy of hinge performance, where the load-path details can be ignored now that the hinge has formed. The accuracy of their expressions however diminishes as the ridge becomes more concentrated: moreover, in the limit of zero width, the expressions become *undefined*.

The developable assumption insists that, whatever the width of the ridge, the cross-section must flatten entirely when a cylindrical hinge forms. But in [6, 7] they observe from careful experiments (and to the contrary) that a narrow ridge remains *pronounced*; there is virtually no change in the original pitch angle despite *most* of the cross-section being flat.

We aim to find accurate expressions for the hinge properties, but we consider only cross-sections with a singular ridge—our *ridge-spring*. A fully curved cross-section is a tape-spring, of course, and the performance of strips with intermediate widths of ridges—as for the CuBe strips in Fig. 1, will lie somewhere between these *extrema*.

We assume from the observation in [6, 7] that the ideal pitch angle remains fixed, and that cylindrical bending of each side panel must comply with this transverse, kinematic boundary condition. Consequently, a narrow strip along the ridge line becomes doubly curved.

There is thus a concentrated (and positive) change in Gaussian curvature within the hinge, which causes in-plane stretching—quite different from inside a tape-spring hinge. Stretching and (out-of-plane) bending must be considered together, whose competition sets the characteristic properties of the hinge. Furthermore, the deformation state does not vary along the hinge *viz.* does not depend on the folded arc-length if the hinge is assumed to be a propagating instability.

Our layout is as follows. More accurate measurements of shape and loads are first obtained from finite element analysis of different ridge-springs. For completeness, we repeat Rimrott's analysis [3] for determining tape-spring hinge properties. This inspires three energetic formulations describing the properties of a folded ridge-spring hinge with increasing detail, which are compared to data from finite element analysis. We also compare the hinge radius and its propagation moment to those from a tape-spring for the sake of efficacy. In our final discussion we show, informally, that local energy minima are not always guaranteed; that hinge propagation depends on the initial geometry.

2 Finite element analysis

Figure 2 shows the bending responses of a ridge-spring and a tape-spring using the commercial finite element analysis package, ABAQUS [8]. As noted, equal and opposite moments, M, are applied to their long ends to cause the tension along the strip centre-line and compression of the free edges: θ is the total rotation between them along the strip.

Both strips are rendered from linear S4R5 shell elements capable of large displacements and rotations [8]. Small strains prevail under a linear elastic material, with the properties of copper beryllium—one of the materials used in Fig. 1. The mesh density for the ridge-spring increases towards its discontinuous ridge line, in order to capture well the rate of rapidly changing local deformation.

The cross-sections of the loaded ends are held rigidly, which simulates their encasement in end blocks *c.f.* Fig. 1. They are free only to rotate in the direction of applied moments and to displace along the strip axis; the rest of strip is otherwise free, and originally free of any stresses.

Geometrical non-linearity is enabled and large displacements follow. A built-in stabilisation option is used in order to "push past" the early unstable buckling phases common in both strips. Their emergence, and settling, corresponds to sharp peaks and troughs in the bending response in Fig. 2.

The initial linear bending quickly softens when the long edges locally buckle symmetrically, close to the ends. These buckles migrate asymmetrically on the free edges when the end rotations are increased, to give torsional displacements before coalescing centrally and symmetrically to form a nascent hinge.

The steady-state hinge moment—our propagation moment—is clearly constant and independent of θ, and is denoted by M^* later. The side views in Figs 2(a) and (b) show, informally, how the arc-lengths of both hinges increase with θ at constant radius of curvature. Their uniform shapes also suggest that the effects of the rigid end constraints are not felt, provided the strips are long enough.

In particular, the natural transition regions that form on either side of the hinge can be accommodated freely within the overall length of strip. Their lengths are non-trivial to find: Rimrott [9], again, estimated as such for a tape-spring, which was recently extended by the author for orthotropic materials [10].

There is no equivalent prediction for a ridge-spring. Therefore, we increased the length of spring for each cross-sectional geometry until the applied moment was observed to be independent of θ and thus unaffected by the rigid ends. If either spring type is too long initially, the analysis may not converge because more edge buckles form, which thwart their eventual coalescence.

Both strip proportions are nominally the same: the ridge and tape have the same length and material thickness, t, and the ridge-spring arc-width, b, is equal to the product of transverse radius, R, and subtended angle, 2α, for the tape-spring, Fig. 2(c). The pitch angle of the ridge line is α, giving a change of inclination of 2α, which expresses the same angularity as the tape-spring cross-section; their structural depths however differ, which sets a larger initial stiffness for the ridge-spring.

The ridge-spring propagation moment is larger by around 3.7 times; conversely, its radius of curvature in side-view is smaller compared to the tape-spring. The inset figures also show, informally, how the in-plane axial stresses vary within each strip. The extent of both hinge shapes is clearly demarcated from the straight side lengths, and a narrow central region of high stresses is present in the ridge-spring.

The analysis was repeated for other ridge-springs with geometries similar to those in Fig. 1: b in the range 10 mm to 40 mm, t from 0.1 mm to 0.4 mm, and pitch angles as 5°, 10° or 15°. Changing the Poisson's ratio exerts little variation and was maintained at a typical value of 0.3 throughout.

Not all geometries, however, afforded convergent solutions, usually when the thickness was smallest or the pitch angle largest; conversely, thicker and shallower strips tended to curve uniformly along their lengths without localising into distinct hinges. Intermediate and, thus, successful geometries are listed finally in Fig. 9.

The folded hinge curvature, κ^*, was measured by averaging the shell curvature along two strips of elements either side of the ridge line: this value is then multiplied by b to give dimensionless $\bar{\kappa}^*$. The propagation moment, M^*, is equal to the end moment and is divided by the product of flexural rigidity, $D = Et^3/12(1-v^2)$, and α, to give $\bar{M}^*$ (henceforth, the "moment"): the Young's modulus is E and the Poisson's ratio is ν.

Given that all hinges form without axial constraint, their properties only depend on b, t and α of the cross-section: α is itself dimensionless (and its inclusion for $\bar{M}^*$ will be clarified soon), thus b/t is the only other dimensionless grouping.

Values of $\bar{\kappa}$ and $\bar{M}^*$, in groups of the same pitch angle, are thence plotted on logarithmic axes in Fig. 3 against the ratio b/t. Each group clearly clusters along individual straight lines, suggesting a power-law relationship to b/t.

The index for each group was determined using a least-squares fit using the software package MATLAB [11]. Accurate values are listed in Fig. 3 but we note that for $\bar{\kappa}$ the range is 0.25 to 0.31, and for $\bar{M}^*$, 0.34 to 0.38. The incremental spacing between successive pairs of fitted lines is also similar for both $\bar{\kappa}^*$ and $\bar{M}^*$, suggesting, informally, a power-law in α.

3 Tape-spring hinge

We repeat the well-known theoretical analysis of a tape-spring hinge [3, 12] in preparation for a ridge-spring.

The folded tape in side-view in Fig. 4(a) shows a hinge radius, r, subtending angle θ. The straight parts on either side do not distort any further once formed in shape, as θ changes. Furthermore, only developable changes in curvature occur within the hinge, for corresponding moments, M^*, applied equally to the ends.

Coordinates x and y are in the transversal and longitudinal directions of the mid-plane of the hinge shell surface, giving changes in curvature, χ, of $\chi_x = -1/R$ and $\chi_y = 1/r$ for the bending direction shown in

Figs 4(b) and (c). This is *equal-sense* bending [4] because the initial and deformed hinge curvatures have their centres on the same side of tape; there is also no twisting curvature.

From [13], the strain energy density per unit surface area of shell can be expressed in terms of the curvature changes as:

$$\frac{D}{2} \cdot \left[\chi_x^2 + \chi_y^2 + 2\nu\chi_x\chi_y\right] \tag{1}$$

Multiplying by the surface area of hinge, $b \cdot r\theta$ (with $b = 2R\alpha$), the total energy stored is U_T, where:

$$U_\mathrm{T} = \frac{D}{2} \cdot br\theta \cdot \left[\frac{1}{R^2} + \frac{1}{r^2} - \frac{2\nu}{rR}\right] \tag{2}$$

This is minimised by setting $\mathrm{d}U/\mathrm{d}r = 0$, which returns $r = \pm R$: the minus sign indicates a valid result when the tape is bent also in the *opposite sense* [4], in accordance with Rimrott's findings. Substituting r, we find U equal to $(Db\theta/R) \cdot (1 - \nu)$, for equal-sense.

Finding M^* recalls from finite element analysis its invariance with θ. When the subtended fold angle of the hinge increases by $\delta\theta$, each end rotates by $\delta\theta/2$. The external work performed by *both* applied moments is thus $2 \cdot (M^* \cdot \delta\theta/2)$, which foists an increase in stored energy, δU: in other words, $\mathrm{d}U/\mathrm{d}\theta = M^*$, which produces

$$M^* = \frac{Db}{R} \cdot (1 - \nu) = 2D\alpha(1 - \nu) \quad \rightarrow \quad \bar{M}^* = 2 - 2\nu \tag{3}$$

after replacing b by $R \cdot 2\alpha$.

The same result for M^* can be found by directly substituting χ_x and χ_y into the generalised Hooke's law for the bending moment (per unit width) along the hinge *i.e.* $M_y = D(\chi_y + \nu\chi_x)$ [13] and multiplying by b for M^*—because the changes in curvature are uniform (the y subscript can be dropped).

4 Ridge-spring hinge: simple model

The initial cross-section is shown again in Fig. 5(a). When the hinge forms, *most* of the cross-section has become flattened except for the ridge line where the pitch angle, α, is preserved.

In schematic side-view, the folded ridge-spring is practically identical to the earlier tape-spring, Fig. 4(a). The hinge, *on average*, has a uniform radius r and connects to straight, transition regions that do not distort with hinge angle, θ; the same in-plane coordinates (x, y) and their directions prevail, see Fig. 5(a).

The elastic shape of hinge can be formed in two stages—after separating each side panel from the ridge line and rotating them to the horizontal plane by equal and opposite angles, α, Fig. 5(b).

Each panel is uniformly bent to a radius r (downwards), Fig. 5(c.i); their inside edges are then locally bent upwards by an applied transverse moment, M_0, per unit length, in order to restore the original pitch

angle, α, whilst the longitudinal radius, r, is *maintained*, Fig. 5(c.ii).

We are thus separating the bending which dominates the global shape from the mid-plane stretching arising from enforcing the correct boundary condition on the ridge. The latter introduces additional transverse bending only when the longitudinal curvature changes are small compared to the thickness and when the ridge-spring is originally straight.

Each effect thus stands alone in terms of the viability of superposing them. The same argument applies, for example, in describing the deformed shape of a bent circular tube which has now ovalised in the so-called Brazier effect, see [13]. Moreover, the order of process here ensures that bending and stretching are decoupled straightforwardly.

The first stage only has a change of longitudinal curvature, $\chi_y = 1/r$, giving a strain energy density, $(D/2)\cdot(1/r^2)$, from Eqn 1. The relationship between α and M_0 is a familiar one from the study of end-loaded cylinders [13]:

$$\alpha = \frac{\mu M_0}{D} \tag{4}$$

where

$$\mu = \frac{(r \cdot t)^{1/2}}{[3(1-\nu)]^{1/4}} \tag{5}$$

Gradients are assumed to be shallow, giving relatively small displacements compared to r, which, nevertheless, accord generator bending across the panel and in-plane hoop-wise stretching along. Practically speaking, this sets maximal gradients to be about 15°, which is our limit for α in the simulations from Section 2.

The corresponding strain energy density per unit arc-length of ridge line is equivalent to the work performed by M_0 when rotated by α, *i.e.* $(1/2)\cdot M_0 \cdot \alpha$, hence, $D\alpha^2/2\mu$ using Eqn 4—a calculation step inspired from [14].

The total strain energy, U_R, multiplies each component by the folded hinge area and the ridge length (on both sides), respectively, to yield:

$$U_\mathrm{R} = \frac{D}{2} \cdot \frac{1}{r^2} \cdot br\theta + \frac{D\alpha^2}{2\mu} \cdot 2r\theta = \frac{Db\theta}{2r} + D\alpha^2\theta \cdot [3(1-\nu^2)]^{1/4} \cdot \left(\frac{r}{t}\right)^{1/2} \tag{6}$$

Minimising U_R with respect to r sets the radius of hinge, r^*, whence:

$$\bar{\kappa}^* = \frac{b}{r^*} = [3(1-\nu^2)]^{1/6} \cdot \alpha^{4/3} \cdot \left(\frac{b}{t}\right)^{1/3} \tag{7}$$

The expression for r^* is substituted back in to U_R, in order to find M^* from $\mathrm{d}U_\mathrm{R}/\mathrm{d}\theta$, which is also equal to U_R/θ (because U_R is linear in θ). After tidying up and dividing by $D\alpha$, we arrive at

$$\bar{M}^* = \frac{M^*}{D\alpha} = \frac{3}{2} \cdot [3(1-\nu^2)]^{1/6} \cdot \alpha^{1/3} \cdot \left(\frac{b}{t}\right)^{1/3} \tag{8}$$

The one-third index of (b/t) in $\bar{\kappa}^*$ and $\bar{M}^*$ matches the general trends in Fig. 3 and will be explored formally later: the surmised power-law variation in α terms is 4/3 and 1/3, respectively (both indices are 4/3 if we do not divide by α for $\bar{M}^*$).

The dimensional performance is clear, which enables a tractable comparison later to a tape-spring. Their compactness stems from the straightforward two-stage bending process, which, however, is incomplete in two ways—which may diminish their accuracy.

Uniform cylindrical bending of each side panel sets the transverse curvature, χ_x, equal to zero and its commensurate bending moment, M_x, equal to $D(\chi_x + \nu\chi_y) = D\nu/r$, *everywhere*, including the inside and outside edges, see Fig. 6(a).

The free (outside) edges of the hinge are thus loaded by fictitious moments, which constrain the overall deformation and artificially increase the total strain energy; these moments must be nullified, thereby *releasing* strain energy. All edge rotations, on the inside and out-, cannot now be zero; as a corollary, the rotation furnished by M_0 is no longer equal to α.

Secondly, the expression for μ, Eqn 5, assumes that the transverse displacements from M_0 have decayed away to zero on the free outer edges. In theory, the width of each panel is infinite but its normal displacements w, Fig. 5(d), are known from [13] to attenuate rapidly over distances of the order μ *i.e.* over approximately $(r \cdot t)^{1/2}$ compared to $b/2$.

A relatively thin panel ensures that major displacements are focused near the edges in narrow *boundary layers*, even though we do not know the value of μ, *a priori*. The matter, however, is compounded when the cylindrical edge moments are nullified, for they produce their own boundary layers. The potential for any coupling across a panel between the applied moments, and their influence upon edge rotations, therefore increases.

Dealing with the fictitious edge moments as proposed is inspired by the approach adopted in [14] for calculating the hinge radius of a folded tape-spring more accurately than Rimrott's result. We assume here, first, that there is no coupling between any of the edge moments, fictitious or not—that boundary layers are narrow; we follow up by not making this assumption.

5 Ridge-spring hinge: enhanced models

The fictitious free edge moments, M_x, are shown in the positive sense of r in Fig. 6(a). Opposing moments, M_1, are applied to the same edges, Fig. 6(b.i), causing all four of them to rotate in the upwards sense by angle ψ: clearly, $M_1 = M_x$ $(= D\nu/r)$ for the outside edges to be free.

The work performed by M_1 is $(1/2) \cdot M_1 \cdot \psi$ per unit length of panel edge, which causes an equal release of stored strain energy. From Eqn 4, $\psi = \mu M_1/D$ equal to $\mu\nu/r$: thus, we subtract from the total strain energy an amount of

$$\frac{1}{2}M_1\psi \cdot 4r\theta = \frac{D\psi^2}{2\mu} \cdot 4r\theta \tag{9}$$

The two inside edges are now rotated from angle ψ to α by the action of M_2, Fig. 6(b.ii). Positive work is performed in this stage whether $\alpha > \psi$, when M_1 off-loading produces a smaller edge rotation than α, or *vice versa*, when the pitch angle is very small.

Shallow gradients, nevertheless, are assumed to remain, resulting in a linear relationship between M_2 and the change in edge rotation, governed similarly to Eqn 4: $M_2 = (D/\mu) \cdot |\alpha - \psi|$. The amount of work from M_2 is equal to $(1/2) \cdot M_2 \cdot |\alpha - \psi|$ and equal to an uptake of stored strain energy.

The modified total strain energy, U_{M}, is therefore

$$U_{\mathrm{M}} = \frac{D}{2} \cdot \frac{1}{r^2} \cdot br\theta + \frac{D}{2\mu} \cdot (\alpha - \psi)^2 \cdot 2r\theta - \frac{D\psi^2}{2\mu} \cdot 4r\theta \tag{10}$$

where the first component is the same cylindrical bending term from Eqn 6.

Substituting for μ from Eqn 5 and re-arranging, we find:

$$U_{\mathrm{M}} = \frac{D\theta}{2}\left[\frac{b}{r} + 2A\sqrt{\frac{r}{t}}\left(\alpha^2 - \psi^2 - 2\alpha\psi\right)\right] \tag{11}$$

with $A = [3(1-\nu^2)]^{1/4}$. Replacing ψ with $\mu\nu/r$

$$U_{\mathrm{M}} = \frac{D\theta}{2}\left[\frac{b}{r} + 2A\left(\alpha^2\sqrt{\frac{r}{t}} - \frac{\nu^2}{A^2}\sqrt{\frac{t}{r}} - \frac{2\alpha\nu}{A}\right)\right] \tag{12}$$

Setting $\mathrm{d}U_{\mathrm{M}}/\mathrm{d}r = 0$ and tidying up, it can be shown that

$$A\alpha^2 \cdot \left(\frac{r}{t}\right)^{3/2} + \frac{\nu^2}{A} \cdot \left(\frac{r}{t}\right)^{1/2} = \frac{b}{t} \tag{13}$$

This cubic polynomial in the group $(r/t)^{1/2}$ is exactly soluble. The closed-form expression for $r = r^*$ is however lengthy and accords an even longer expression for M^* when r^* is substituted in $\mathrm{d}U_{\mathrm{M}}/\mathrm{d}\theta$ $(= U_{\mathrm{M}}/\theta)$: both expressions are not immediately useful.

Alternatively, a typical value of A is 1.29 for $\nu = 0.3$, making $A\alpha^2$ and ν^2/A of similar size. The second left-side term is smaller than the first by a factor of r/t and is negligible if r is much larger than t—when the ridge-spring is thin. Consequently:

$$r = r^* = \left[\frac{b^2 t}{A^2\alpha^4}\right]^{1/3} \quad \rightarrow \quad r^* = \frac{b^{2/3} \cdot t^{1/3}}{[3(1-\nu^2)]^{1/6} \cdot \alpha^{4/3}} \tag{14}$$

which is precisely our standard (dimensioned) result from Eqn 7.

Substituting $r = r^*$ into $\mathrm{d}U_{\mathrm{M}}/\mathrm{d}\theta$ (equal to U_{M}/θ), we find, after some algebra:

$$\bar{M}^* = \frac{M}{D\alpha} = -2\nu + \frac{3}{2} \cdot A^{2/3} \cdot \alpha^{4/3} \cdot \left(\frac{b}{t}\right)^{1/3} - \frac{\nu^2}{\alpha^{1/3} \cdot A^{2/3}} \cdot \left(\frac{t}{b}\right)^{1/3} \tag{15}$$

Formal predictions are given later but the range of ridge-spring geometries used in Section 2 sets the second term to be the largest in value (which is also equal to $\bar{M}^*$ from the simpler model, Eqn 8). The third term is much smaller, evidently because it varies with t/b not b/t. The size of -2ν is, however, not negligible, and the term is retained.

The term -2ν also features in $\bar{M}^*$ for a tape-spring, recall Eqn 3. Here it is due to M_2 rotating by $\alpha - \psi$ (and not by α alone), even if ψ itself is very small; accounting for the fictitious edge moments is ultimately responsible. Thus, with reasonable accuracy, we may set $\bar{M}^*$ equal to:

$$\bar{M}^* = -2\nu + \frac{3}{2} \cdot [3(1-\nu^2)]^{1/6} \cdot \alpha^{1/3} \cdot \left(\frac{b}{t}\right)^{1/3} \tag{16}$$

The actions of M_1 and M_2 stipulate independent rotations α and ψ when their displacements decay rapidly; or when the panel width, $b/2$, is much larger than $(r \cdot t)^{1/2}$. Because we are solving for r, we do not know if this condition is upheld; if not, the moments and rotations couple to each other across the panel, where now M_1 affects α and ψ, as does M_2.

The general case and their positive directions, from [13], is shown in Fig. 6(c). The dimensionless moments, m, and rotations, ϕ, are related to the full quantities, M and ψ, by [13]

$$m = \frac{\mu^2 M}{2D}, \quad \phi = \mu\psi \tag{17}$$

with μ defined originally by Eqn 5. Labelling the ends of the cylinder by A and B, the particular relationships from [13] can be verified as

$$m_{\mathrm{A}} = \frac{1}{2} \cdot (-p\phi_{\mathrm{A}} + q\phi_{\mathrm{B}}], \quad m_{\mathrm{B}} = \frac{1}{2} \cdot [-q\phi_{\mathrm{A}} + p\phi_{\mathrm{B}}) \tag{18}$$

where

$$p = (\sinh 2\xi + \sin 2\xi)/k, \quad q = 2(\cosh\xi \sin\xi + \sinh\xi \cos\xi)/k \tag{19}$$

with

$$k = \cosh 2\xi - \cos 2\xi \quad \text{and} \quad \xi = (b/2)/\mu \tag{20}$$

The parameter, ξ, is the ratio of the side-panel width to boundary-layer width; when the coupling between edge moments is weak, the boundary layers are narrow and $\xi >> 1$.

Returning to the case of Fig. 6(b.i), we set $m_{\mathrm{A}} = m_{\mathrm{B}} = m_1$ and $\phi_{\mathrm{A}} = -\phi_{\mathrm{B}} = -\phi_1$. Substituting into Eqns 18, we find

$$m_1 = \frac{1}{2} \cdot (p+q)\phi_1 \quad \rightarrow \quad M_1 = \frac{D\psi_1}{\mu} \cdot (p+q) \tag{21}$$

For the case of Fig. 6(b.ii), $m_{\mathrm{B}} = 0$, which sets $\phi_{\mathrm{B}} = (q/p) \cdot \phi_{\mathrm{A}}$. Substituting back into m_{A}, noting $m_{\mathrm{A}} = m_2$, re-arranging and re-normalising:

$$M_2 = \frac{D\psi_2}{\mu} \cdot \left(p - \frac{q^2}{p} \right) \tag{22}$$

The previous work arguments can now be applied.

Fictitious edge moments, M_1, equal to $D\nu/r$, are released and cause both ends of each panel to rotate by ψ, equal to ψ_1. The ridge line moments, M_2, enable the inside edges to rotate further by ψ_2 equal to $\psi - \alpha$, and perform positive work. The now exact stored strain energy, denoted as U_{E}, can be written as (*c.f.* Eqn 10):

$$U_{\mathrm{E}} = \frac{D}{2} \cdot \frac{1}{r^2} \cdot br\theta + \frac{D}{2\mu} \cdot (\psi - \alpha)^2 \cdot 2r\theta \cdot \left(p - \frac{q^2}{p} \right) - \frac{D\psi^2}{2\mu} \cdot 4r\theta \cdot (p + q) \tag{23}$$

The (p, q) terms inside parenthesis can be expanded and simplified marginally to give

$$p - \frac{q^2}{p} = \frac{\cosh 2\xi + \cos 2\xi - 2}{\sinh 2\xi + \sin 2\xi}, \quad p + q = \frac{\sinh \xi + \sin \xi}{\cosh \xi - \cos \xi} \tag{24}$$

U_{E} is highly nonlinear (because μ, *viz.* r, is "embedded" in ξ inside hyperbolic functions). We do not attempt to simplify further, and values of r that minimise U_{E} are found numerically.

For confirmation, note that $p - q^2/p$ and $p + q$ both tend to unity when ξ is much greater than unity (for narrow boundary layers). The moments effectively decouple from each other, and U_{E} reads the same as U_{M} in Eqn 10.

6 Results

The predictions for $\bar{\kappa}^*$ and $\bar{M}^*$ are compared with each other in Fig. 7 before we compare to finite element data.

The ordinate axis for $\bar{\kappa}^*$ is set to $\alpha^{4/3} \cdot (b/t)^{1/3}$: the simplest prediction from Eqn 7 therefore plots as a straight line. The ordinate range is set by ridge-spring geometries from finite element analysis, which are individually detailed in Fig. 9; throughout $\nu = 0.3$.

Numerical solutions of $\bar{\kappa}^*$ are found by using the approximate value of r^* from Eqn 14 to specify a range of (fine) values for r about r^*. The corresponding variation of U_{M}, Eqn 10, (which is independent of θ) is searched for a stationary value using a standard routine in MATLAB [11]: r^* is then adjusted from Eqn 14, whence $\bar{\kappa}^* = b/r^*$.

Values of $\bar{\kappa}^*$ for each ridge-spring geometry are plotted in Fig. 7 and follow Eqn 7 almost identically; such closeness justifies solving Eqn 13 approximately, as described previously.

The solution process is repeated for U_{E} and the plotted results are, again, close to Eqn 7. However, two of the initial geometries given by $(b, t, \alpha) = (10, 0.2, 5^\circ)$ and $(10, 0.4, 10^\circ)$ yield no stable minima and hence no solutions. These points are absent compared to them from U_{M} at ordinate values of 0.14 and 0.29.

The variations of $\bar{M}^*$ are plotted against ordinate axis of $\alpha^{1/3} \cdot (b/t)^{1/3}$ given Eqn 8, which forms the dashed line in Fig. 7: the parallel line offset by 2ν below is Eqn 16.

From earlier, $\mathrm{d}U_{\mathrm{M}}/\mathrm{d}\theta$ is equivalent to U_{M}/θ. Thus, the stationary values of U_{M} found numerically directly specifies values of M^*; we may do the same with U_{E} in Eqn 23. Both variations are practically equal to Eqn 16 with the missing result points both occurring when the ordinate reads 1.63.

There is practically no difference between the simple estimates of $\bar{\kappa}^*$ and $\bar{M}^*$ and their more elaborate solution values, so we may use Eqn 7 ($\bar{\kappa}^*$) and Eqn 16 ($\bar{M}^*$) confidently in order to compare to the finite element data. The absent data points, however, demand discussion—see later.

The same ordinate groups are maintained in Fig. 8. The curvature results tend to show more scatter but both sets of finite element data evidently cluster in linear fashion. The importance of the 2ν offset is also clear for $\bar{M}^*$.

The differences between the finite element data and theory are quantified directly in Fig. 9 by re-plotting their ratios as discrete data points in vertical *silos* pertaining to the same shape of strip. The thickness of strip increases from left to right in each silo, and we plot two sets of ratios, using the exact solutions and the simplified closed-form expressions.

The curvature ratios mostly lie between unity and 1.1, with some values above but not exceeding 1.22; one exceptional ratio below unity is 0.92. The moment ratios are broadly contained between unity and 1.06, with no values above 1.1.

The differences arising from the two theoretical approaches are slight with the simplified curvature predictions showing more variation within a narrower band, 0.92 to 1.18. On average, the simplified moment behaves *better* than the exact solution, giving moment ratios closer to unity in general.

7 Comparison to tape-spring

The hinge properties do not depend on the strip lengths for both a tape- and ridge-spring. When comparing them, we conserve the amount of cross-sectional material, which sets b equal to $R \cdot 2\alpha$, for the same thickness, t. The subtended angularity is the same, which, as noted, leads to a higher bending stiffness initially for the ridge-spring—for interest elsewhere see *e.g.* [6].

A direct comparison is facilitated by expressions in closed form. The case for hinge curvature is thus straightforward using Eqn 7. Denoting each curvature as κ^*_{RS} and κ^*_{TS} (RS: ridge-spring; TS: tape-spring), it can be verified that

$$\frac{\kappa^*_{\mathrm{RS}}}{\kappa^*_{\mathrm{TS}}} = \frac{[3(1-\nu^2)]^{1/6}}{2^{2/3}} \cdot \left(\frac{R}{t}\right)^{1/3} \cdot \alpha^{2/3} \tag{25}$$

For $\nu = 0.3$, the pre-factor above is very close to 3/4. The ridge-tape hinge curvature is greater (*viz.* radius is smaller) than that of the tape-spring when $(R/t) \cdot \alpha^2 > (4/3)^3$ (=2.37). A tape-spring has a typical ratio of $R/t = 100$, thus a ridge-spring is more tightly folded when $\alpha > 9°$.

Similarly, the ratio of moments M^*_{RS} (Eqn 16) and M^*_{TS} (Eqn 3) can be verified as

$$\frac{M^*_{\mathrm{RS}}}{M^*_{\mathrm{TS}}} = \frac{3}{4} \cdot \frac{2^{1/3} \cdot [3(1-\nu^2)]^{1/6}}{(1-\nu)} \cdot \left(\frac{R}{t}\right)^{1/3} \cdot \alpha^{2/3} - \frac{\nu}{(1-\nu)} \tag{26}$$

A ratio greater than unity sets the condition

$$(3/4) \cdot 2^{1/3} \cdot [3(1-\nu^2)]^{1/6} \cdot (R/t)^{1/3} \cdot \alpha^{2/3} > 1 \tag{27}$$

which returns $(R/t) \cdot \alpha^2 > 0.72$ when $\nu = 0.3$, *i.e.* a lower threshold compared to the curvature case: when $R/t = 100$ (again), $\alpha > 5°$ specifies a larger hinge moment for the ridge-spring. In the case of Fig. 2, Eqn 26 returns 3.33 for the moment ratio, which is around 11% smaller than the finite element comparison of 3.7.

8 Discussion

A ridge-spring focuses the transverse curvature of a tape-spring into a pitched ridge line. It can be folded into a fixed radius of curvature which propagates the arc-length of hinge, similar to a tape-spring.

The hinge properties of the latter, however, are much simpler in their variation. The hinge radius is equal to the original transverse radius, and the dimensionless hinge moment depends only on the angle subtended by the cross-section (for a fixed Poisson's ratio), as proposed by Rimrott [3].

A folded ridge-spring hinge behaves non-linearly with b, t and α, where its dimensionless curvature and absolute moment depend on $\alpha^{4/3} \cdot (b/t)^{1/3}$. Compared to a tape-spring, there is more variety in ridge-spring dependencies, with more freedom to tailor hinge properties and, hence, to improve performance for applications.

As the tape-spring hinge radius compares to its original cross-sectional value, we might ask when the hinge radius of a ridge-spring is equal to, for example, the flattened width *i.e.* when $\bar{\kappa}^* = 1$. Reading from Fig. 7, $\alpha^{4/3} \cdot (b/t)^{1/3} \approx 0.85$, which sets $\alpha \approx 16°$ when b/t takes a typical value of 100.

A wide range of finite element simulations have correlated well with predictions of hinge curvature and moment, especially for the latter. We note, however, that the accuracy of predictions decreases when the material thickness increases: in each silo in Fig. 9 the departure from unity appears to increase in general, moving left to right.

The geometry of the hinge is expected to be mostly cylindrical *i.e.* developable, except near the ridge line. This is truer in relatively thinner shells that inhibit the build-up of in-plane forces [15]. Thicker shells are, conversely, less developable, which erodes the uniform extent of the cylindrical hinge shape. Its radial shape may vary, and appreciably so, across the width, producing the scatter we see in the finite element data—for $\bar{\kappa}^*$ at least.

However, this argument also depends on the pitch angle *c.f.* the deformed cross-sectional profiles in Fig. 10. Even though both strips have the highest thickness of $t = 0.4$ mm, the hinge cross-section with the larger pitch angle ($\alpha = 15°$) has mostly flattened; a smaller pitch angle ($\alpha = 5°$) leads to a conical cross-section. Both ridge lines, however, are much stiffer than the panels, with no discernible opening across them; for different loading cases when this is no longer a valid assumption see [16].

This figure also shows that there is, potentially, a reasonable height difference between the ridge centre-line, where $\bar{\kappa}^*$ is measured from finite element analysis, and the outside edges, which trace the side profile of the hinge in our schematic view, when measured relative to the side-panel widths. A better estimate of an "average" hinge radius may be to measure this radius of curvature directly in side view.

Most remarkably, the enhanced models give very similar results to them from the basic model. But recall that there are (two) absent results in Fig. 9 (and Fig. 7) where energy minima are not found for two strip geometries.

We examine the strain energy behaviour for one of them in Fig. 11, from silo C, where $b = 10$ mm, $\alpha = 5°$ and $t = 0.2$ mm. Two other nearby thicknesses are considered, $t = 0.1$ mm and 0.15 mm, and the corresponding dimensionless variations ($\bar{U} = U/D\theta$) of U_R (Eqn 6), U_M (Eqn 10) and U_E (Eqn 23) around their minima are plotted.

The minima from U_R and U_M are clearly stable for all thicknesses: analytically, we may validate, for example, that the discriminant of Eqn 13 is positive whatever the cross-sectional properties, which signifies a positive real root—always.

The behaviour from U_E, however, is highly sensitive to thickness, with the minimum profile disappearing altogether when $t = 0.2$ mm. Even though there is little "lateral" movement in the value of r^* beforehand (which assures the concurrencies of Fig. 7), edge effects now dominate and overwhelm any stable hinge formation.

The broader behaviour is given in Fig. 12 which first shows a contour map of the hinge radius that minimises U_E, for the indicated axes ranges of b/t and α. We normalise the radius by dividing by r^* from Eqn 14 and thus observe, largely, a ratio of unity.

There is, however, a region of insoluble initial geometries (that do not form hinges) separated by a boundary front from radii ratios that dip below unity, rise above and settle down, over a short range moving into the map from the origin outwards. Remarkably, this boundary is well described by $\alpha = 350/(b/t)$; and it would be interesting to see if the same division also applies to performances from (many more) finite element

analysis.

Figure 12 also shows the equivalent contour map via U_{M} from Eqn 10. None of the normalised radii are larger than unity although the contours have a similar shape and, importantly, the map is populated *everywhere*; U_{M} always has a local minimum. Even though there are no significant differences in the hinge radii predicted either by U_{M} or U_{E}, their stability can be quite differently assured.

We have deliberately avoided varying the Poisson's ratio, for the sake of brevity. It is important for $\bar{M}^*$ to be accurate *c.f.* the difference of 2ν between Eqns 8 and 16, but its contribution in Eqn 13 is dominated by the pitch angle term when proper edge moments are considered.

The recent tape-spring study [14] shows that the Poisson's ratio significantly alters the folded hinge radius expected from Rimrott's prediction. Without delving details, one reason is the simultaneous changes in curvature along the hinge *and* across the tape during cylindrical bending. Our singular ridge-spring does not experience this, but if another ridge-spring has a finite central ridge, as tested in [7], the Poisson effect may be significant. We leave this to further study.

References

[1] M G Walker and K A Seffen, On the shape of bistable creased strips, *Thin-Walled Structures* (2018) 124, pp. 538-545

[2] K A Seffen, *Analysis of Structures Deployed by Tape-Springs* (1997) PhD Dissertation, University of Cambridge

[3] F P J Rimrott, Querschnittsverformung bei Torsion offener Profile, *Zeitschrift für Angewandte Mathematik und Mechanik* (1970) 50, pp. 775-778

[4] K A Seffen and S Pellegrino, Deployment dynamics of tape-springs, *Proceedings of the Royal Society of London, A* (1999) 455, pp. 1003-1048

[5] S Kyriakides, Propagating instabilities in structures, *Advances in Applied Mechanics*, (1993) 30, pp. 67189

[6] M G Walker and K A Seffen, The flexural mechanics of creased strips, *International Journal of Solids and Structures* (2019) 167, pp. 192-201

[7] M G Walker, *Flexural Mechanics of Creased Thin Metallic Strips* (2018) PhD Dissertation, University of Cambridge

[8] Hibbitt and Karlsson and Sorensen, *ABAQUS/Standard User's Manual, Version 6.14* (2014)

[9] V K Jain and F P J Rimrott, The ploy region of a slit tube, *Canadian Aeronautics and Space Institute (CASI) Transactions* (1971) 4(2), pp. 140-144

[10] K A Seffen and B Wang and S D Guest, Folded orthotropic tape-springs, *Journal of the Mechanics and Physics of Solids* (2019) 123, pp. 138-148

[11] *MATLAB Release 2013b* (2013) The MathWorks, Inc., Natick, Massachusetts, United States

[12] C R Calladine, The theory of thin shell structures 1888-1988: Love Centenary Lecture, *Proceedings of the Institute of Mechanical Engineers* (1988) 202, pp. 141-149

[13] C R Calladine, *Theory of Shell Structures* (1983), Cambridge University Press

[14] C R Calladine and K A Seffen, Folding the carpenter's tape: boundary layer effects, *Journal of Applied Mechanics: accepted* (2019)

[15] E H Mansfield, *The Bending and Stretching of Plates* (1988), Cambridge University Press

[16] F Lechenault and B Thiria and M Adda-Bedia, Mechanical response of a creased sheet, *Physical Review Letters* (2014) 112, paper 244301

Figures

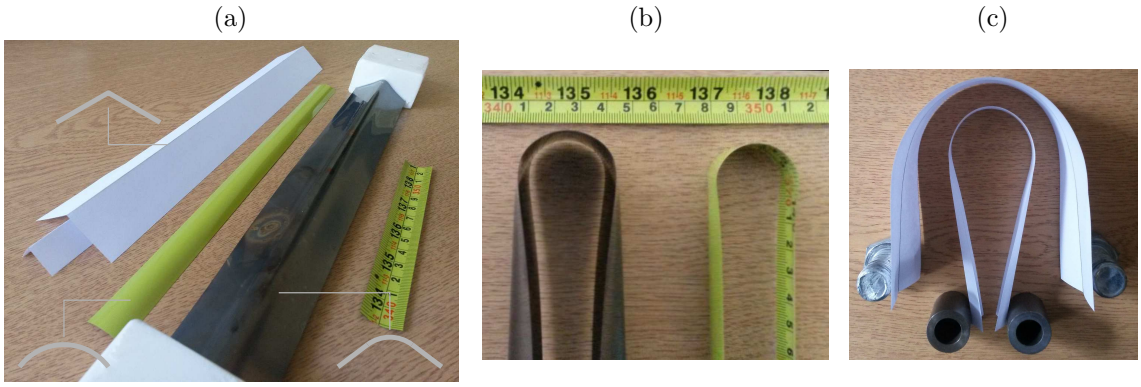

FIGURE 1: (a) Strip with three types of cross-sectional shape: sharply bent paper ridges (white) and flat side panels; bent copper beryllium strip (50 mm arc-width, 0.125 mm thickness) with distributed ridge width, set in end blocks; uniformly curved, standard carpenter's tapes. (b) Metal strips from (a) bent longitudinally to form localised cylindrical hinge of approximately constant radius of curvature. (c) Paper strips from (a) also bent to form central hinge. The original strips only differ in their widths: note their different cylindrical radii.

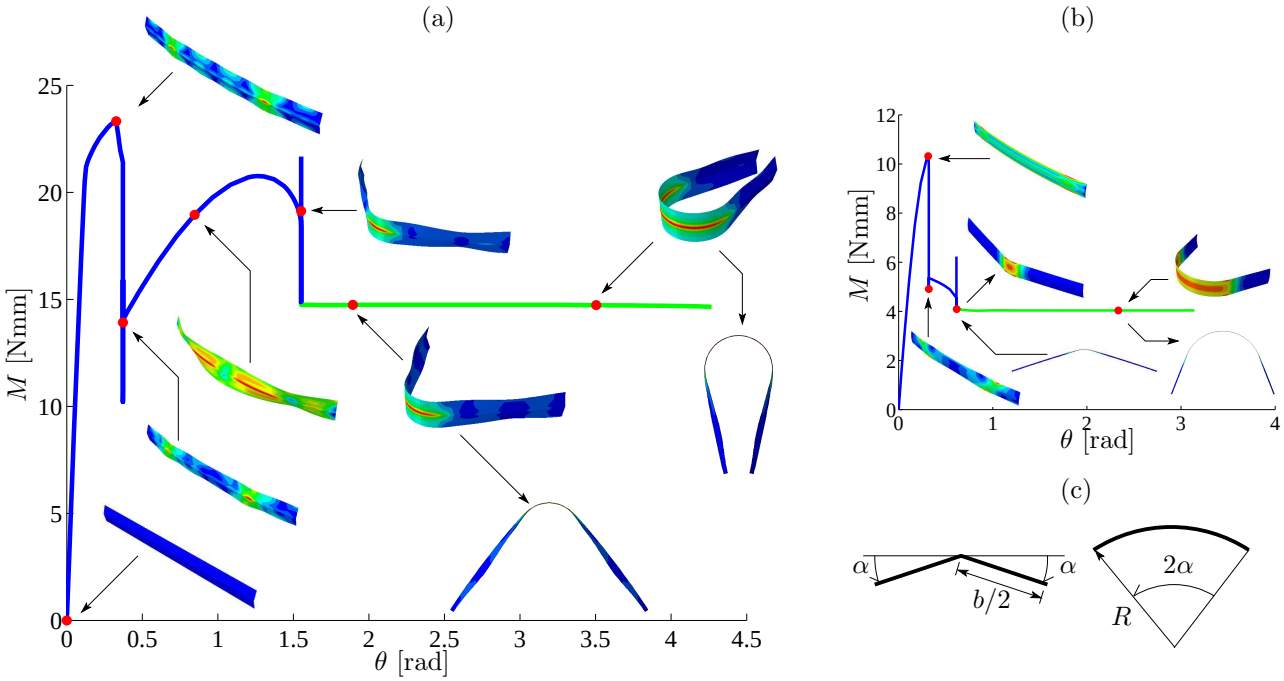

FIGURE 2: Finite element analysis of moment-rotation (M, θ) response of (a) ridge-spring and (b) tape-spring using ABAQUS [8]. For inset geometry: $b = 10$ mm, $R = 19.10$ mm, $\alpha = 15°$ and $t = 0.1$ mm. Strip lengths are $L = 100$ mm and material properties have $E = 131$ GPa and $\nu = 0.3$ (of copper beryllium). Deformed geometries correlate with the highlighted dots (red); blue curves are initial linear phases followed by non-linear buckling with torsion; constant moment responses are green lines where each central circular hinge region maintains constant radius as their hinge fold angles θ increase.

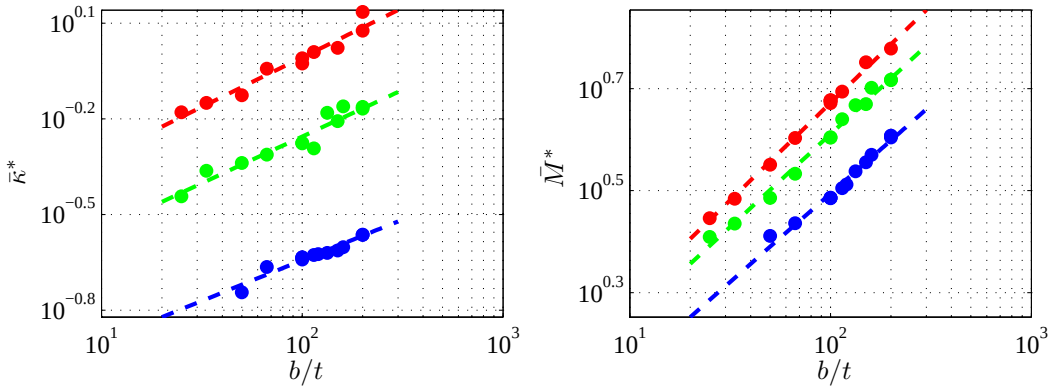

FIGURE 3: Numerical fitting (dashed lines) of dimensionless results (dots) from finite element analysis. Each data set is a different pitch angle; $\alpha = 5°$ (blue), $\alpha = 10°$ (green), $\alpha = 15°$ (red). Values of power-law indices for (b/t) variation are: $(\bar{\kappa}^*)$ 0.2551 (b), 0.2928 (g), 0.3108 (r); $(\bar{M}^*)$ 0.3463 (b), 0.3634 (g), 0.3813 (r). Fitting uses a standard least-squares function in MATLAB [11].

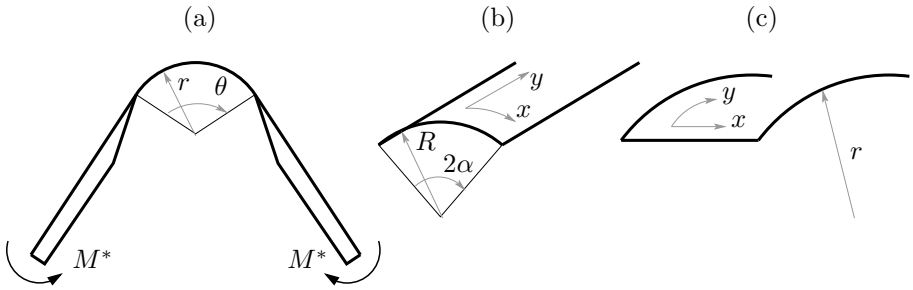

FIGURE 4: (a) Schematic of bent tape-spring in side view with central hinge of radius r and subtended fold angle θ: equal and opposite moments M^* applied to the far ends. (b) Initial cross-sectional geometry; in-plane coordinates (x, y) are transverse and longitudinal; (c) cylindrical hinge region.

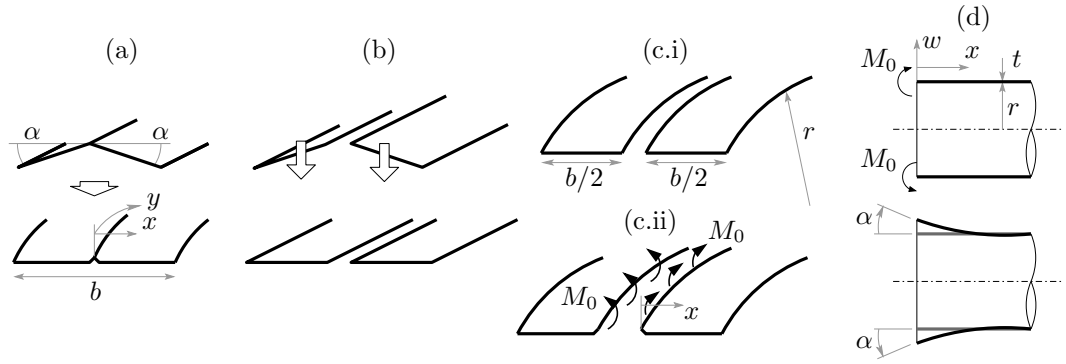

FIGURE 5: Formation sequence of (nearly) cylindrical hinge for ridge-spring. (a) Initial and final cross-sectional shapes. (b) Separation of side panels and their rigid-body rotation to horizontal. (c.i) Uniform cylindrical bending of side panels to radius r; (c.ii) application of moment M_0 on inside edges to restore the original pitch angle α. (d) Cylindrical bending analogue for effect of M_0 on single panel; w are radial displacements.

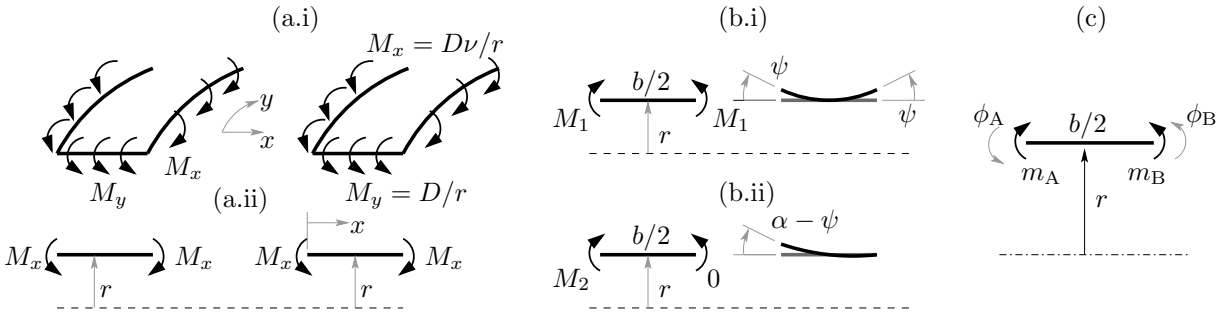

FIGURE 6: Correction of hinge equilibrium in Fig. 5. (a.i) Uniformly bent side panels with non-zero edge moments M_x; (a.ii) cross-sectional views. (b.i) Correcting moments M_1 applied in reverse on panel edges (only the right side-panel is shown) and their symmetrical edge rotations ψ; (b.ii) further bending of inside edges by M_2 to pitch angle α. (c) Bending of narrow cylinder by general edge moments, m_A and m_B, and their corresponding rotations, ϕ_A and ϕ_B.

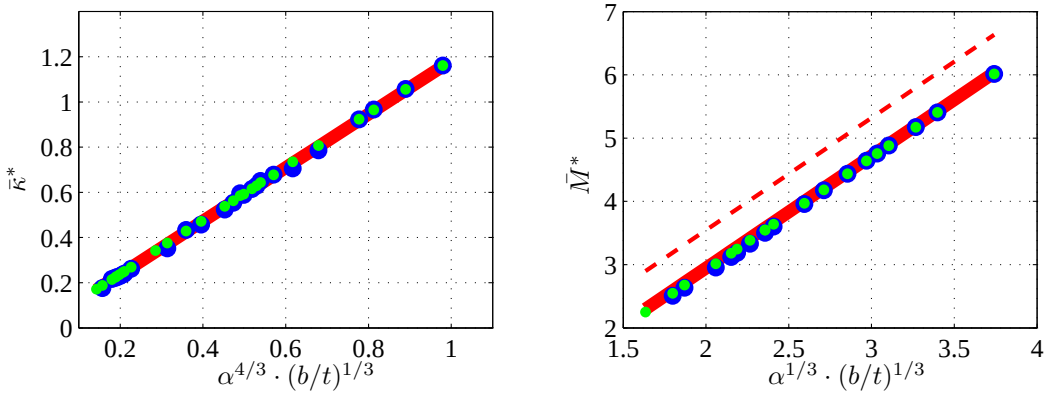

FIGURE 7: Comparison of theoretical predictions: left, hinge curvature; right, hinge moment. Thick red lines are closed-form solutions from Eqn 7, left, and Eqn 16, right; both lines extrapolate through each origin. Dashed line, right, is Eqn 8. Smaller green dots (dealing with exact free edges) from solving Eqn 10 numerically; larger blue dots (on coupling of edge moments) from Eqn 23. Ordinate ranges set by geometries used in Fig. 9.

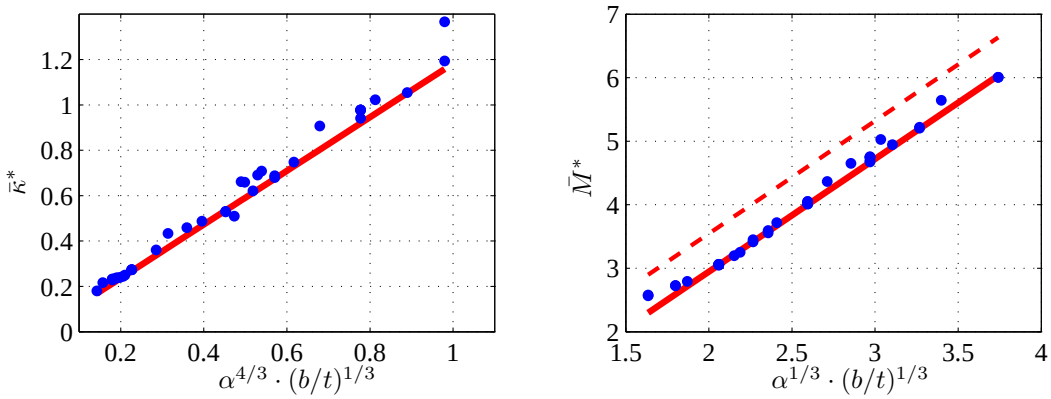

FIGURE 8: Comparison of hinge curvature, left, and moment, right, from finite element analysis, dots, to theoretical predictions, Eqns 7 and 16 (solid lines): dashed line is Eqn 8. Respective ordinate axes are the same as in Fig. 7 and initial geometries are given in Fig. 9.

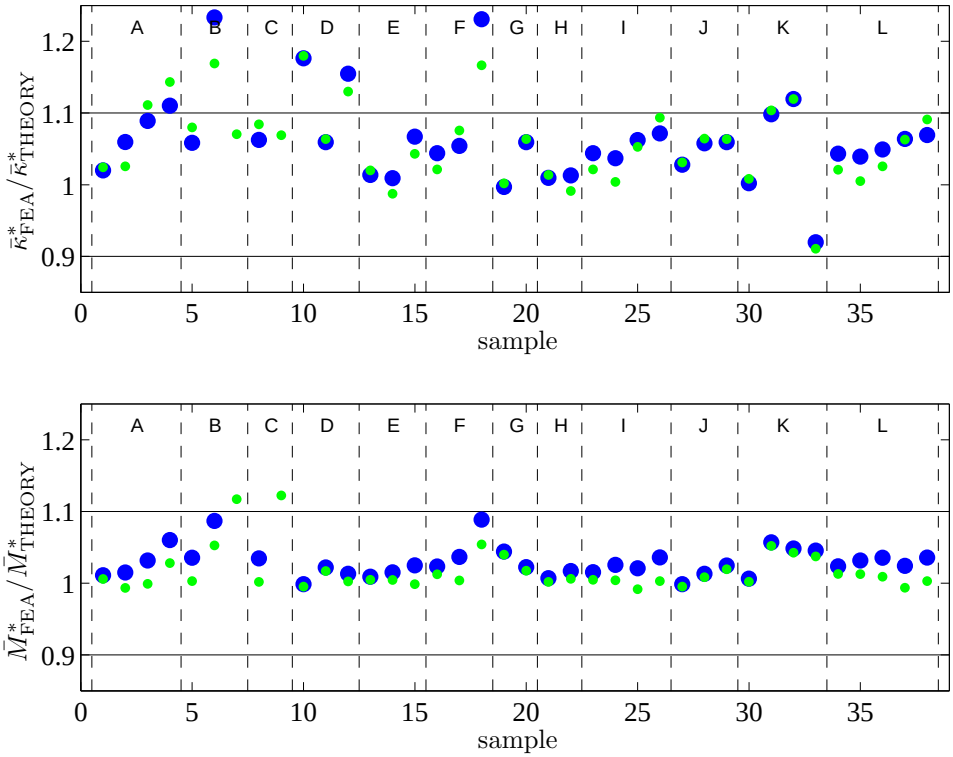

FIGURE 9: Comparison of finite element analysis and theory for hinge curvature, top, and moment, bottom. Larger blue dots use exact strain energy, $U_{\rm E}$; smaller green dots from Eqns 7 and 16. Vertical silos, A ... L, for different ridge-spring cross-sections (b, α, t, L) of units (mm, °, mm, mm): L is length of each finite element specimen. In each silo, the thickness increases ($\rightarrow$) in steps of 0.1 mm except for silos I, K and L, where the step is 0.05 mm. A (10, 15, 0.1 $\rightarrow$ 0.4, 100); B (10, 10, 0.2 $\rightarrow$ 0.4, 150); C (10, 5, 0.1 $\rightarrow$ 0.2, 300); D (20, 15, 0.1 $\rightarrow$ 0.3, 100); E (20, 10, 0.1 $\rightarrow$ 0.3, 200); F (20, 5, 0.1 $\rightarrow$ 0.3, 400); G(30, 15, 0.2 $\rightarrow$ 0.3, 150); H (30, 10, 0.2 $\rightarrow$ 0.3, 250); I (30, 5, 0.15 $\rightarrow$ 0.3, 600); J (40, 15, 0.2 $\rightarrow$ 0.4, 200); K (40, 10, 0.2 $\rightarrow$ 0.35, 300); L (40, 5, 0.2 $\rightarrow$ 0.4, 750).

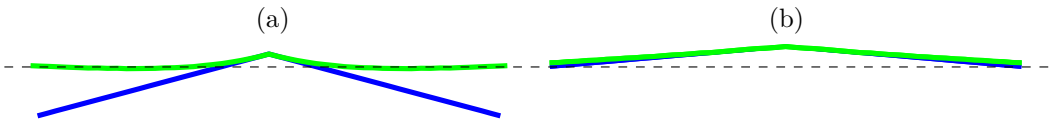

FIGURE 10: Deformed hinge cross-sections (green) in folded ridge-springs: initial cross-section (blue). (a) $b = 10$ mm, $t = 0.4$ mm and $\alpha = 15°$. (b) $b = 10$ mm, $t = 0.4$ mm and $\alpha = 5°$.

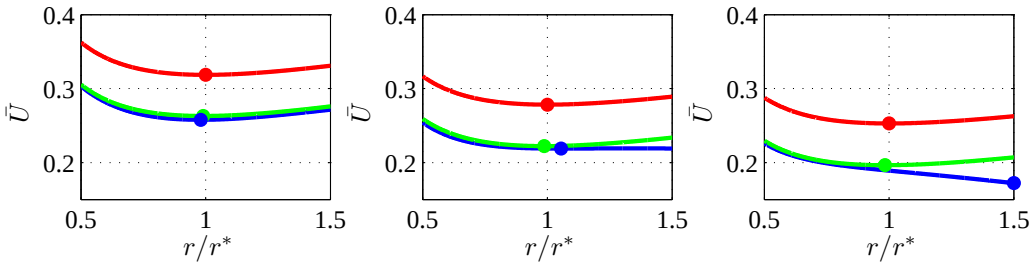

FIGURE 11: Variation in (dimensionless) strain energy with hinge radius for the same ridge-spring (b = 10 mm, $\alpha = 5°$, $\nu = 0.3$) with increasing thickness; t = 0.1 mm, 0.15 mm, 0.2 mm, left to right. Local minima are shown as dots for U_{R} (Eqn 6, red), U_{M} (Eqn 10, green) and U_{E} (Eqn 23, blue). Final minimum point from U_{E} is not stationary.

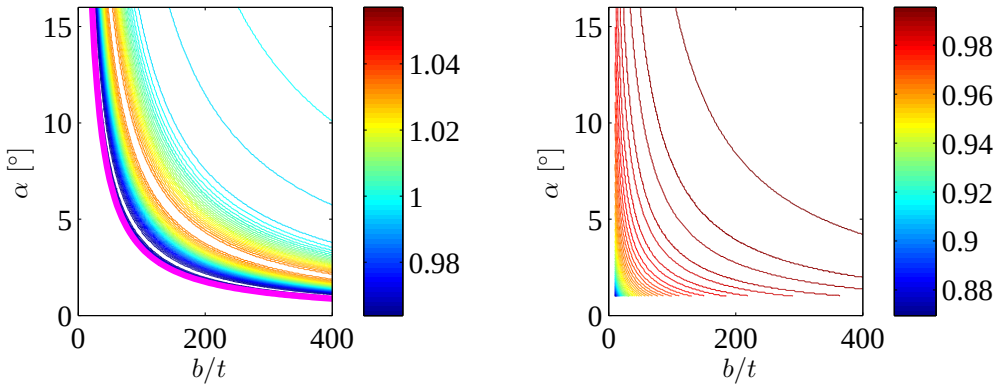

FIGURE 12: Contour maps of viable hinge radius (divided by r^*, Eqn 14) via U_{E} (left) and U_{M} (right): minimum values of α and b/t ranges are 1° and 10, respectively. No solutions exist below and to the left of the purple boundary for U_{E}, which is approximately given by $\alpha = 350/(b/t)$ (when $\nu = 0.3$).